

**Oscillations and confluence in three-magnon scattering of ferromagnetic resonance**Tao Qu<sup>1</sup>, Alex Hamill<sup>2,\*</sup>, R. H. Victora<sup>1</sup>, and P. A. Crowell<sup>2</sup><sup>1</sup>*Department of Electrical and Computer Engineering, University of Minnesota, Minneapolis, Minnesota 55455, USA*<sup>2</sup>*School of Physics and Astronomy, University of Minnesota, Minneapolis, Minnesota 55455, USA*

(Received 12 April 2022; revised 8 August 2022; accepted 6 January 2023; published 3 February 2023)

We have performed a time-resolved and phase-sensitive investigation of three-magnon scattering of ferromagnetic resonance (FMR) over several orders of magnitude in excitation power. We observe a regime that hosts transient oscillations of the FMR magnon population, despite higher-order magnon interactions at large powers. Also at high powers, the scattering generates 180° phase shifts of the FMR magnons. These phase shifts correspond to reversals in the three-magnon scattering direction, between splitting and confluence. These scattering reversals are most directly observed after removing the microwave excitation, generating coherent oscillations of the FMR magnon population much larger than its steady-state value during the excitation. Our model is in strong agreement with these findings. These findings reveal the transient behavior of this three-magnon scattering process, and the nontrivial interplay between three-magnon scattering and the magnons' phases.

DOI: [10.1103/PhysRevB.107.L060401](https://doi.org/10.1103/PhysRevB.107.L060401)

Magnons are the quanta of collective spin excitations. Their phase degree of freedom, highly nonlinear behavior [1–17], and long lifetimes make them an active subject in fundamental research [18–21] and research towards next-generation microwave and information technology [22–29]. A magnon mode's population (hereafter referred to as its amplitude) can be excited above a threshold value such that it becomes unstable, returning to the threshold value through three-magnon splitting [30]. This nonlinear process is referred to as the first-order Suhl instability.

The zero-wave-vector magnon mode corresponds to ferromagnetic resonance (FMR) and has a dramatically low threshold amplitude for this instability, particularly in magnetic insulators due to their low damping. This allows for efficient excitation of finite-wave-vector magnons and the study of nonlinear magnon interactions over a wide power range. However, little is known about how this instability evolves in time and the role of the excitation power. Previous experiments have observed no associated power dependence [31], or have instead focused on the influence of dipole radiation [32] or of group velocity and proximity to the excitation antenna [33]. The reverse process of splitting is referred to as confluence, which also requires further investigation [33]. Its relationship with splitting is an unresolved question, as is the relationship between three-magnon scattering processes and the magnons' phases.

To this end, we employ time-resolved homodyne spectroscopy to examine this instability with phase-sensitivity over five orders of magnitude in microwave excitation power. We observe a regime hosting power-dependent transient oscillations of the FMR amplitude, where at high powers the instability induces 180° phase shifts of FMR, and that

these phase shifts correspond to reversals between three-magnon splitting and confluence. Furthermore, turning off the microwave excitation stimulates such reversals, generating prolonged and coherent oscillations of the FMR amplitude. Our model is in strong agreement with these observations, and explains the origin of the oscillatory regime as well as the oscillations after turn-off. The oscillatory regime persists up to the highest powers employed, being remarkably robust against the higher-order interactions that arise.

The FMR mode  $b_0$  with a frequency  $f_0$  is subject to the first-order Suhl instability when magnon modes  $b_{\pm\mathbf{k}}$  at  $f_0/2$  are available. This occurs at low FMR frequencies for in-plane magnetized films, due to a minimum in the magnon dispersion [34,35]; an increase in wave number suppresses the dynamic demagnetization field. With these modes available,  $b_0$  becomes unstable above a threshold amplitude and undergoes three-magnon splitting to  $b_{\pm\mathbf{k}}$ . In the reverse process, confluence, two magnons  $b_{\pm\mathbf{k}}$  combine into a magnon  $b_0$  [Fig. 1(a)].

We investigated this instability in the time domain through homodyne spectroscopy [Fig. 1(b)]. The microwave excitation at the desired FMR frequency  $f_0$  is converted to the desired applied microwave power  $P_a$  and to 8  $\mu\text{s}$  pulses using an attenuator and switch. These pulses enter a wide microstrip waveguide, generating a spatially uniform microwave magnetic field of amplitude  $h_a$  throughout the sample: A 3  $\mu\text{m}$ -thick film of yttrium iron garnet (YIG). We resonantly excite the sample's FMR mode by matching its FMR frequency with  $f_0$ , via tuning the static magnetic field  $H$  to  $H_0$ . We primarily investigated the transient behavior at  $f_0 = 1.5$  GHz, with a corresponding resonant field of  $H_0 = 135$  Oe. The sample is inductively coupled to the microstrip, such that its FMR response  $b_0$  induces a corresponding voltage in the microstrip [36]. We obtain the envelope of the

\*hamil483@umn.edu

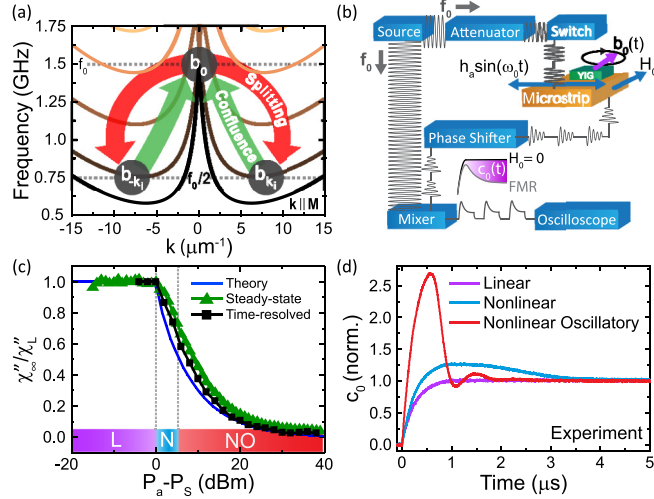


FIG. 1. (a) The magnon dispersion of 3  $\mu\text{m}$  YIG films magnetized in-plane, in  $15^\circ$  increments of the angle between the wave vector  $\mathbf{k}$  and the static magnetization  $\mathbf{M}$ . (b) Schematic diagram of the experiment. (c)  $\chi''_\infty(P_a)/\chi''_L$  predicted from Suhl's theory (blue) and that measured through lock-in techniques (green) and time-resolved measurements (black) at 1.5 GHz. The color-coded regions correspond to the Linear (L), Nonlinear (N), and Nonlinear Oscillatory (NO) regimes. (d) Overview of the transient behavior of the FMR magnon population  $c_0$  in each regime at 2.5 GHz, normalized to the values of  $c_0$  at steady state.

microstrip's output voltage by mixing it with a phase- and frequency-matched reference. By subtracting the output voltage's envelope at resonance from that at zero field, we isolate the envelope of the voltage induced by FMR. When nonlinearity-induced phase shifts are absent, this envelope directly corresponds to the FMR amplitude  $c_0(t)$  with the susceptibility  $\chi''(t) = c_0(t)/h_a \propto c_0(t)/\sqrt{P_a}$ . For additional experimental details, see Sec. 1 of the Supplemental Material (SM) [37] and Ref. [38] therein.

To verify our experiment, we compare the measured steady-state susceptibility  $\chi''_\infty$  with Suhl's theory [30] around the instability's threshold power  $P_S$  [see Fig. 1(c)]. For  $P_a < P_S$ ,  $c_0$  is in the linear regime, such that its steady-state value is proportional to  $h_a$ . For  $P_a = P_S$ , this value corresponds to  $c_S$ , the threshold amplitude for the (nonlinear) instability regime. The steady-state value of  $c_0$  saturates at  $c_S$  in the nonlinear regime, as three-magnon splitting occurs for  $c_0 > c_S$ . As such, as  $P_a$  is increased,  $\chi''_\infty$  decreases as  $\chi''_\infty \propto 1/\sqrt{P_a}$ . We compare this with the experimental results by normalizing  $\chi''_\infty$  to its value in the linear regime  $\chi''_L$ . The experimentally obtained saturation from both steady-state (using lock-in techniques) and time-resolved measurements is in reasonable agreement with the theoretical prediction.

In our time-resolved measurements [Fig. 1(d)], we find both the linear and nonlinear regimes as well as their expected transient behavior: in the linear regime (purple curve)  $c_0$  rises monotonically to its steady-state value, while in the nonlinear regime (blue curve) it becomes unstable and then relaxes to  $c_S$  via three-magnon splitting. However, we observe an additional regime with a threshold power  $P_{\text{osc}} > P_S$ , in which  $c_0$  oscillates at a power-dependent frequency as it relaxes to  $c_S$  (red curve).

To understand this regime, we have developed a model for three-magnon scattering of FMR in thin films, for the case of resonant excitation by a perpendicular microwave field (see Sec. 2 of SM [37] for details). We derive the associated equation of motion for the circularly-polarized magnetization  $m^+$  via the Landau-Lifshitz equation. We then perform a plane-wave expansion of  $m^+$  [30] to obtain the equations of motion of the circularly precessing magnon modes. Afterwards, we employ a classical Bogoliubov transformation [39] to obtain the equations of motion of the eigenmodes, the elliptically precessing magnon modes  $b(\mathbf{k})$ . We only retain terms up to second order in the magnon modes, to account for three-magnon scattering while neglecting higher-order interactions. We account for linear damping of  $b(\mathbf{k})$  through the relaxation rate  $\eta(\mathbf{k}) = \omega(\mathbf{k})\epsilon(\mathbf{k})\alpha$  [40];  $\omega(\mathbf{k})$  is the mode's angular frequency,  $\epsilon(\mathbf{k}) = \frac{1}{\gamma}(\partial\omega/\partial H)|_{\mathbf{k}, H_0}$  is the ellipticity factor,  $\gamma$  is the gyromagnetic ratio, and  $\alpha$  is the measured Gilbert damping constant. We only consider the resulting equations of motion of the FMR mode  $b_0$  and the  $N_k$  magnon modes  $b_k$  of frequency  $f_0/2$  in the magnon dispersion. Each of these half-frequency modes' equation of motion is distinguished by  $\zeta_k$ , their coupling strength with  $b_0$ , and their relaxation rate  $\eta_k$ . However, these distinguishing parameters have weak variation among the  $f_0/2$  modes. Hence, we set  $\zeta_k$  and  $\eta_k$  to their average value over all  $f_0/2$  modes,  $\bar{\zeta}$ ,  $\bar{\eta}_k$ . This causes the equations of motion for each of the half-frequency modes to be identical, reducing the  $N_k$  half-frequency modes to a single effective mode  $b_k$ . Note that we also equate  $b_k(t)$  and  $b_{-k}(t)$ , as the splitting and confluence processes affect each mode equally. This reduces our model to the two equations of motion

$$\dot{b}_0 = (i\omega_0 - \eta_0)b_0 - N_k \bar{\zeta} b_k^2 + \nu h_a e^{i(\omega_0 t - \pi/2)}, \quad (1)$$

$$\dot{b}_k = (i\omega_k - \bar{\eta}_k)b_k + \bar{\zeta} b_k^* b_0. \quad (2)$$

$\nu$  is the coupling of  $b_0$  to the microwave field. The magnon mode's response  $b_i$  ( $i = 0, k$ ) encodes both its amplitude  $|b_i|$  and its phase, such that  $b_i(t) = |b_i(t)|e^{i(\omega_i t + \theta_i + \phi_i(t))}$ .  $\theta_{0,k} = -\pi/2, -\pi/4$  are the modes' phase offsets for the cases of linearity and weak nonlinearity, as found from numerically solving Eqs. (1) and (2).  $\phi_i(t)$ , discussed later, will correspond to phase shifts induced by strong nonlinearity. We define  $c_i(t)$  as the mode's amplitude for  $\phi_{0,k} = 0$ , such that  $b_i(t) = c_i(t)e^{i(\omega_i t + \theta_i)}$ . Inserting this relation into Eqs. (1) and (2) yields the equations of motion for the magnon mode amplitudes:

$$\dot{c}_0 = -\eta_0 c_0 - N_k \bar{\zeta} c_k^2 + \nu h_a, \quad (3)$$

$$\dot{c}_k = -\bar{\eta}_k c_k + \bar{\zeta} c_k c_0. \quad (4)$$

This definition of  $c_0$ , as in the experiment, corresponds to the envelope of  $b_0$  obtained by mixing it with a frequency-matched reference signal  $e^{-i(\omega_0 t + \theta_0)}$ . As such, the experiment can be directly compared with the numerical solutions of Eq. (3). For numerically solving our equations of motion, we set the value of  $h_a$  such that  $h_a/h_S$  matches the experiment and simulations;  $h_S$  is the observed threshold value of  $h_a$  for the instability.  $\eta_i$  is calculated as described previously. All other parameters are set to the values calculated from our model. See Sec. 2 of SM [37] for their derivations. The initial values are the thermal amplitudes corresponding to the Bose-Einstein distribution (see Sec. 3 of SM [37]). For details

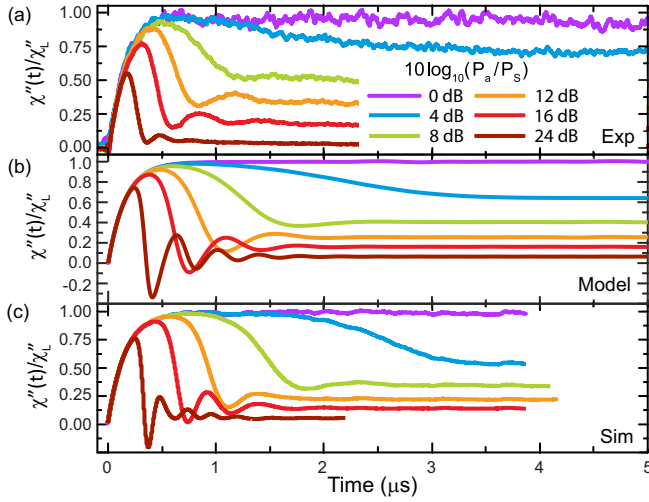


FIG. 2. Comparison of the FMR amplitude's transient behavior at 1.5 GHz from (a) the experiment, (b) the numerical solutions to Eqs. (3),(4), and (c) the micromagnetic simulations. The FMR amplitude  $c_0$  is normalized to  $\chi''(t)/\chi_L''$  to enable direct comparison between each approach.

on the simulations and numerical solutions, see Sec. 4 of SM [37] and Refs. [41–45] therein.

Figure 2 compares the time evolution of  $c_0$  from the experiment, the numerical solutions of Eqs. (3),(4), and the micromagnetic simulations. We normalize to  $\chi''(t)/\chi_L''$  for direct comparison between each approach. Each curve color corresponds to the same relative power  $P_a/P_S$ . The purple and blue curves correspond to the linear and nonlinear regimes, while the green curves correspond to the entrance into the nonlinear oscillatory regime. As  $P_a$  is increased, the oscillation frequency  $f_{\text{osc}}$  monotonically increases while the time scale of the initial transient peak monotonically decreases. Strong qualitative agreement is observed between each approach, which is also the case at 2.5 GHz (see Sec. 5 of SM [37]). The oscillations weaken as one goes from the model to simulation to experiment, presumably due to increasing magnon dephasing. In addition to simulations allowing for other magnon interactions, they include thermal fluctuations which can lead to dephasing. In the experiment, additional dephasing may arise from sample and magnetic field inhomogeneity.

To analyze the oscillatory regime, we linearize Eqs. (3) and (4) by Taylor expanding  $\dot{c}_0, \dot{c}_k$  about the nonlinear regime's fixed point, which corresponds to steady state; this allows us to treat the second-order terms as negligible. We then impose a time dependence of the form  $c_0, c_k \propto e^{\lambda t}$ , and solve for  $\lambda$ . The transition to the oscillatory regime corresponds to the nonlinear regime's fixed point changing from a stable node to a stable spiral, such that  $\lambda$  becomes complex. This transition can be thought of as the point where the splitting rate becomes large enough to produce negative feedback by suppressing  $c_0$  to below  $c_S$ , where splitting is suppressed. This generates exchanges in dominance between the splitting and the microwave excitation terms in Eq. (3), hence the oscillations. This analysis (see Sec. 6 of SM [37]) yields predicted values for the oscillation frequency  $f_{\text{osc}}$  and the threshold value of  $h_a$

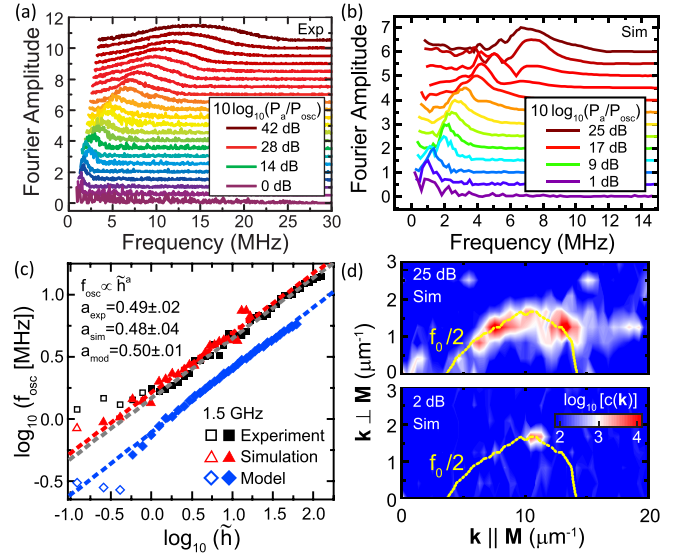


FIG. 3. Oscillation analysis at  $f_0 = 1.5$  GHz. (a), (b) Normalized and offset frequency spectra of the oscillations in (a) the experiment, and (b) the simulations, with a 2 dB increment between curves. (c) The scaling of the oscillation frequency  $f_{\text{osc}}$  for each approach. The filled symbols indicate the fitted region and have a spacing of 1 dB in power. (d) The simulations' magnon mode amplitudes  $c(\mathbf{k})$  for powers 2 dB (bottom, no broadening) and 25 dB (top, with broadening) greater than  $P_{\text{osc}}$ .

for the oscillatory regime,  $h_{\text{osc}}$ :

$$f_{\text{osc}} = \eta_0 \sqrt{\frac{\tilde{\zeta} v}{8\pi^2}} (h_a - h_{\text{osc}}), \quad (5)$$

$$h_{\text{osc}} = h_S \left( 1 + \frac{\eta_0}{8\tilde{\eta}_k} \right). \quad (6)$$

We compare the predicted scaling from Eq. (5) with our results by extracting, via a Fourier transform, the oscillations' frequency spectra from each approach [Figs. 3(a) and 3(b)]. We define  $f_{\text{osc}}$  at each power as the characteristic peak in the oscillations' frequency spectra and  $h_{\text{osc}}$  as the value of  $h_a$  just below where low-frequency structure is observed in the spectra. For more details, see Sec. 7 of SM [37]. The linearized model's predicted scaling  $f_{\text{osc}} \propto \tilde{h}^{0.5}$ , where  $\tilde{h} = (h_a - h_{\text{osc}})/h_{\text{osc}}$ , is compared to the scaling obtained from each approach [Fig. 3(c)]. We normalize  $h_a - h_{\text{osc}}$  by  $h_{\text{osc}}$  to directly compare each approach. The model's results are from the numerical solutions of Eqs. (3) and (4). The filled symbols are those included in the scaling fit (dashed lines) such that quantitative agreement with Eq. (5) is observed. The range of agreement for each approach is several orders of magnitude in  $P_a$ . This is also the case for  $f_0 = 2.5$  GHz (see Sec. 5 of SM [37]). The oscillation frequencies in the experiment and simulations show good agreement, but they are larger than those from our model. This is likely due to an incomplete treatment of damping and/or an underestimation of  $\tilde{\zeta}$ , as we neglect the full Gilbert damping term and spatial variation of the longitudinal magnetization component.

As the relative power  $10 \log_{10}(P_a/P_{\text{osc}})$  increases to 14 dB, the oscillations' frequency spectra broaden in the experiment

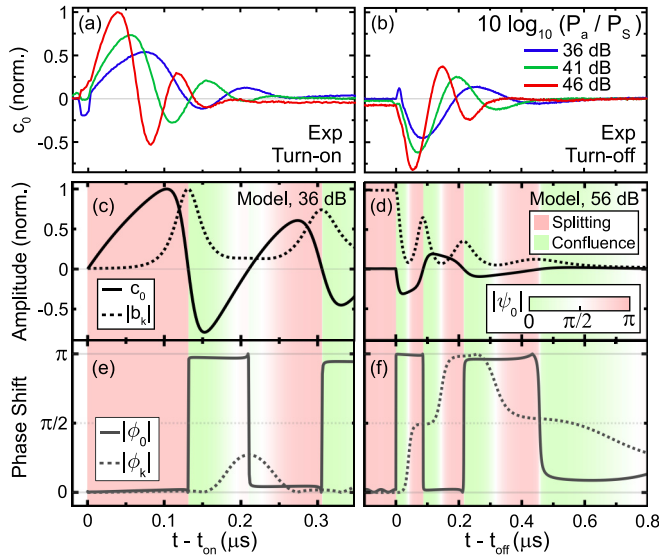


FIG. 4. (a), (b) The experimental results for  $c_0(t)$  at high powers when turning on and off the microwave excitation at 1.5 GHz. Each curve is normalized to the peak amplitude at turn-on for the relative power of 46 dB. (c), (d) The magnon amplitudes  $c_0$ ,  $|b_k|$ , with each time color-coded for the corresponding value of  $|\psi_0|$ . Note that  $c_0$  at turn-off is instead normalized to the peak amplitude at turn-on for the relative power of 56 dB. (e), (f) The corresponding phase shifts  $|\phi_{0,k}|$ .

and simulations [Figs. 3(a) and 3(b)]. To investigate this, we compare the simulations' magnon mode amplitudes  $c(\mathbf{k})$  [46] at the relative powers of 2 dB (no broadening) and 25 dB (pronounced broadening) [Fig. 3(d)]. At 2 dB, only the  $f_0/2$  modes with the largest coupling strengths  $\zeta_k$  are excited. Note that the coupling is strongest for the modes with wave vectors most misaligned with the static magnetization  $\mathbf{M}$ . At 25 dB, the weaker-coupled  $f_0/2$  modes are also excited, with some even exceeding the amplitude of the strongest-coupled modes. The excited modes also exhibit a wider frequency distribution about  $f_0/2$ , which may generate the observed broadening. The most straightforward explanation for this transition is the onset of four-magnon scattering of  $f_0/2$ , opposite-wave-vector pairs of magnons at the strongest-coupled modes, which conserves energy and momentum.

At the highest powers, the splitting becomes pronounced enough to introduce negative values of  $c_0$  [Figs. 4(a) and 4(b)]. As  $c_0$  is phase sensitive, being obtained by mixing  $b_0$  with a reference signal, this corresponds to  $b_0$  undergoing a phase shift  $\phi_0 \sim 180^\circ$ . Phase shifts for the mode  $b_i$  arise when its response is dominated by its scattering term [see Eqs. (1) and (2)], such that it is strongly nonlinear. At these powers, we also observe pronounced oscillations of  $c_0$  after turning off the microwave excitation. Notably, these oscillations' amplitudes greatly exceed the steady-state value of  $c_0$  during excitation and they persist for roughly 600 ns. Each curve in Figs. 4(a) and 4(b) is normalized to the turn-on peak at the highest power, showing the oscillations at excitation turn-on and turn-off to be comparable in size. To understand these observations, we examine the case of strong nonlinearity in our

model by numerically solving Eqs. (1),(2), which provides the evolution of the modes' amplitudes as well as their phases. We calculate the modes' phase shifts  $\phi_i(t)$  by using our general definition  $b_i(t) = |b_i(t)|e^{i(\omega_i t + \theta_i + \phi_i(t))}$ :

$$\phi_i(t) = \frac{1}{i} \ln \left( \frac{b_i(t)}{|b_i(t)|} e^{-i(\omega_i t + \theta_i)} \right). \quad (7)$$

The evolution of the amplitudes and phase shifts is shown in Figs. 4(c) and 4(d) and Figs. 4(e) and 4(f); we utilize  $|\phi_i(t)|$  for simplicity. For consistency with the experiment, we plot  $c_0$  instead of  $|b_0|$ , taking  $c_0(t) = \text{Re}(b_0(t)e^{-i(\omega_0 t + \theta_0)})$ .

After turning on the excitation [Figs. 4(c) and 4(e)], we find  $\pi$  phase shifts of  $\phi_0$  at  $c_0 = 0$ , with these phase shifts triggering variation in  $\phi_k$ . We first examine the influence of the  $\pi$  phase shift on the amplitudes' equations of motion. Whereas  $c_i(t)$  is the mode's amplitude for  $\phi_{0,k} = 0, 0$ , we define  $c'_i(t)$  as the mode's amplitude for  $\phi'_{0,k} = \pi, 0$ . Substituting  $b_i(t) = c'_i(t)e^{i(\omega_i t + \theta_i + \phi'_i)}$  into Eqs. (1) and (2) yields the amplitudes' new equations of motion given the  $\pi$  phase shift:

$$\dot{c}'_0 = -\eta_0 c'_0 + N_k \bar{\zeta} c_k'^2 - \nu h_a, \quad (8)$$

$$\dot{c}'_k = -\bar{\eta}_k c'_k - \bar{\zeta} c'_k c'_0. \quad (9)$$

Comparison with Eqs. (3) and (4) shows that the  $\pi$  phase shift switches the sign of both the microwave field term  $\nu h_a$  and the three-magnon scattering terms  $\sim \bar{\zeta}$ . From the latter, it is evident that these phase shifts correspond to reversals in the three-magnon scattering direction between splitting and confluence. These reversals explain why the phase shifts cause  $|b_k(t)|$  to switch between growing and decaying with time, and why  $|c_0(t)|$  increases with time for  $c_0 < 0$  despite being out-of-phase with (and hence, damped by) the microwave field [Figs. 4(a) and 4(c)]. Furthermore, the reversals explain the variation of  $\phi_k$ : with  $|b_k(t)|$  being suppressed by confluence, its three-magnon scattering term dominates over its linear terms such that  $b_k$  enters the strong nonlinearity regime.

These reversals are more directly evident after turning off the microwave excitation, where  $|c_0(t)|$  undergoes a pronounced increase in time despite the absence of the excitation field. Furthermore, without the microwave field to drive  $\phi_0$  back to  $0^\circ$ , the variations of  $\phi_k$  evolve into  $90^\circ$  phase shifts of  $b_k$ , generating additional reversals [Figs. 4(d) and 4(f)]. The  $180^\circ, 90^\circ$  phase shifts of  $b_0, b_k$  are those required to reverse the scattering direction, with the factor-of-two difference being due to the same factor difference in their frequencies. These reversals explain both the pronounced oscillations of  $c_0$  at turn-off and the oscillations' enhancement with microwave power: the scattering at turn-off, and hence the reversals, are driven by the steady-state values of  $c_0, c_k$  during turn-on, where  $c_k \propto \sqrt{h_a - h_S}$  at steady state [see Eq. 51 in the SM [37]]. The model's turn-off oscillations of  $c_0$  are much weaker than those in the experiment, hence the use of the higher relative power of 56 dB. This may be because of our use of a linear damping term  $-\eta_i b_i$ , which is insensitive to phase shifts, instead of the full Gilbert damping term.

To determine how the scattering direction evolves in time, we consider the relative phase  $|\psi_i(t)|$  between  $b_i$  and the three-magnon scattering term in its equation of motion. As with the linear damping term  $-\eta_i b_i$ , the damping of  $b_i$  by scattering corresponds to the scattering term being  $\pi$

out-of-phase with  $b_i$ . Conversely, the scattering term drives  $b_i$  when it is in-phase with  $b_i$ . As such,  $|\psi_0| = 0, \pi$  corresponds to confluence and splitting, respectively, and we can calculate  $|\psi_0(t)|$  to determine the evolution of the scattering direction. Note that  $|\psi_0(t)|$  and  $|\psi_k(t)|$  are found to mirror each other about  $\pi/2$  as expected, such that one mode is being driven by scattering while the other mode is being damped. From Eq. (1),  $\psi_0(t)$  takes the form

$$\psi_0(t) = \frac{1}{i} \ln \left( \frac{b_0(t)/|b_0(t)|}{b_k^2(t)/|b_k^2(t)|} \right). \quad (10)$$

$|\psi_0(t)|$  corresponds to the color-coding in Figs. 4(c)–4(f). The switching of  $|\psi_0(t)|$  between  $0, \pi$  aligns with the phase shifts and the transitions between growth and decay of  $|b_k(t)|$  as expected, verifying that the relative phase  $|\psi_i(t)|$  indicates the three-magnon scattering direction.

In summary, for three-magnon scattering of ferromagnetic resonance, we observe a regime that hosts transient oscillations of the magnon populations, with the transient behavior being highly dependent on the excitation power. At high excitation powers, we find that the scattering generates sig-

nificant phase shifts of the magnons and that these phase shifts correspond to reversals between three-magnon splitting and confluence. Such reversals also occur upon turning off the excitation, generating prolonged and coherent oscillations. Our model captures these behaviors. These findings shed light on the transient behavior of this instability, and reveal the nontrivial interplay between three-magnon scattering and the magnons' phases.

The authors thank A. Venugopal for fruitful discussion on efficient computation in the micromagnetic simulations and C. D. Schimming for valuable mathematical insight. The Minnesota Supercomputing Institute (MSI) provided resources that contributed to the research results reported within this article. The authors acknowledge support by SMART, a center funded by nCORE, a SRC program sponsored by NIST. The authors also acknowledge support by DARPA under Grant No. W911NF-17-1-0100, the Center for Micromagnetics and Information Technology (MINT) at the University of Minnesota, and the NSF through the Extreme Science and Engineering Discovery Environment (XSEDE) under Grant No. ACI-1548562. T.Q. and A.H. contributed equally to this work.

- 
- [1] S.M. Rezende and F.M. de Aguiar, Spin-wave instabilities, auto-oscillations, and chaos in yttrium-iron-garnet, *Proc. IEEE* **78**, 893 (1990).
- [2] P. Wigen, R. McMichael, and C. Jayaprakash, Route to chaos in the magnetic garnets, *J. Magn. Magn. Mater.* **84**, 237 (1990).
- [3] I. Laulicht and P. Wigen, On the transient and stationary parametric excitation of spin waves, *J. Magn. Magn. Mater.* **207**, 103 (1999).
- [4] C. Mathieu, V.T. Synogatch, and C.E. Patton, Brillouin light scattering analysis of three-magnon splitting processes in yttrium iron garnet films, *Phys. Rev. B* **67**, 104402 (2003).
- [5] S.Y. An, P. Krivosik, M.A. Kraemer, H.M. Olson, A.V. Nazarov, and C.E. Patton, High power ferromagnetic resonance and spin wave instability processes in Permalloy thin films, *J. Appl. Phys.* **96**, 1572 (2004).
- [6] P. Kabos, G. Wiese, and C. E. Patton, Measurement of Spin Wave Instability Magnon Distributions for Subsidiary Absorption in Yttrium Iron Garnet films by Brillouin Light Scattering, *Phys. Rev. Lett.* **72**, 2093 (1994).
- [7] A. Krawiecki and A. Sukiennicki, On-off intermittency and peculiar properties of attractors in a simple model of chaos in ferromagnetic resonance, *Acta Phys. Pol. A* **88**, 269 (1995).
- [8] T.L. Carroll, L.M. Pecora, and F.J. Rachford, Chaos in magnetostatic modes in an yttrium iron garnet film between 2 and 4 GHz, *J. Appl. Phys.* **67**, 5630 (1990).
- [9] T.L. Carroll, L.M. Pecora, and F.J. Rachford, Chaos and chaotic transients in an yttrium iron garnet sphere, *Phys. Rev. A* **40**, 377 (1989).
- [10] T.L. Carroll, L.M. Pecora, and F.J. Rachford, Chaotic Transients and Multiple Attractors in Spin-Wave Experiments, *Phys. Rev. Lett.* **59**, 2891 (1987).
- [11] W. Araujo, F. de Aguiar, A. Azevedo, and S. Rezende, Dual pumping of magnetostatic and spin-wave modes in yttrium-iron-garnet spheres, *J. Appl. Phys.* **93**, 8752 (2003).
- [12] G. Srinivasan, M. Chen, and C. Patton, Observation of auto-oscillations and chaos in subsidiary absorption in yttrium iron garnet, *J. Appl. Phys.* **64**, 5480 (1988).
- [13] V.E. Zakharov, V. L'vov, and S. Starobinets, Spin-wave turbulence beyond the parametric excitation threshold, *Sov. Phys. Usp.* **17**, 896 (1975).
- [14] V.B. Cherepanov and A.N. Slavin, Collective spin-wave oscillations in finite-size ferromagnetic samples, *Phys. Rev. B* **47**, 5874 (1993).
- [15] S. Rezende, F. de Aguiar, and A. Azevedo, Spin-wave auto-oscillations still in need of a good model, *J. Appl. Phys.* **67**, 5624 (1990).
- [16] A.N. Slavin, G. Srinivasan, S. Cordone, and V.B. Cherepanov, Instability mechanism of collective spin wave oscillations in finite-size ferrite samples, *J. Appl. Phys.* **75**, 5610 (1994).
- [17] V.T. Synogach, Y.K. Fetisov, C. Mathieu, and C.E. Patton, Ultrashort Microwave Pulses Generated Due to Three Magnon Interactions, *Phys. Rev. Lett.* **85**, 2184 (2000).
- [18] Roman V. Verba, Lukas Körber, Katrin Schultheiss, Helmut Schultheiss, Vasil Tiberkevich, and Andrei N. Slavin, Theory of three-magnon interaction in a vortex-state magnetic nanodot, *Phys. Rev. B* **103**, 014413 (2021).
- [19] I. Barsukov, H. K. Lee, A. A. Jara, Y.-J. Chen, A. M. Gonçalves, C. Sha, J. A. Katine, R. E. Arias, B. A. Ivanov, and I. N. Krivorotov, Giant nonlinear damping in nanoscale ferromagnets, *Sci. Adv.* **5**, eaav6943 (2019).
- [20] K. Schultheiss, R. Verba, F. Wehrmann, K. Wagner, L. Körber, T. Hula, T. Hache, A. Kákay, A. A. Awad, V. Tiberkevich, A. N. Slavin, J. Fassbender, and H. Schultheiss, Excitation of Whispering Gallery Magnons in a Magnetic Vortex, *Phys. Rev. Lett.* **122**, 097202 (2019).
- [21] T. X. Zhou, J. J. Carmiggelt, L. M. Gächter, I. Esterlis, D. Sels, R. J. Stöhr, C. Du, D. Fernandez, J. F. Rodriguez-Nieva,

- F. Büttner, E. Demler, and A. Yacoby, A magnon scattering platform, *Proc. Natl. Acad. Sci. USA* **118**, e2019473118 (2021).
- [22] A.A. Serga, A.V. Chumak, B. Hillebrands, YIG magnonics, *J. Phys. D* **43**, 264002 (2010).
- [23] J.D. Adam and S.N. Stitzer, Frequency selective limiters for high dynamic range microwave receivers, *IEEE Trans. Microw. Theory Tech.* **41**, 2227 (1993).
- [24] J.D. Adam and F. Winter, Magnetostatic wave frequency selective limiters, *IEEE Trans. Magn.* **49**, 956 (2013).
- [25] P. Pirro, V.I. Vasyuchka, A.A. Serga, and B. Hillebrands, Advances in Coherent Magnonics, *Nat. Rev. Mater.* **6**, 1114 (2021).
- [26] A. Barman *et al.*, The 2021 magnonics roadmap, *J. Phys. Cond. Matt.* **33**, 413001 (2021).
- [27] G. Csaba, Á. Papp, and W. Porod, Perspectives of using spin waves for computing and signal processing, *Phys. Lett. A* **381**, 1471 (2017).
- [28] A.V. Chumak, Magnon spintronics: Fundamentals of magnon-based computing, in *Spintronics Handbook: Spin Transport and Magnetism*, 2nd ed. (CRC Press, Boca Raton, FL, 2019), pp. 247–302
- [29] A. Etesamirad, R. Rodriguez, J. Bocanegra, R. Verba, J. Katine, I. Krivorotov, V. Tyberkevych, B. Ivanov, and I. Barsukov, Controlling magnon interaction by a nanoscale switch, *ACS Appl. Mater. Interfaces* **13**, 20288 (2021).
- [30] H. Suhl, The theory of ferromagnetic resonance at high signal powers, *J. Phys. Chem. Solids* **1**, 209 (1957).
- [31] R. Cunha, J. Holanda, L. Vilela-Leão, A. Azevedo, R. Rodríguez-Suárez, and S. Rezende, Nonlinear dynamics of three-magnon process driven by ferromagnetic resonance in yttrium iron garnet, *Appl. Phys. Lett.* **106**, 192403 (2015).
- [32] B. Desormière, E. Milot, and H. Le Gall, Transient processes in spin-wave systems with magnetic dipole radiation-II. Experimental investigations, *J. Phys. Chem. Solids* **30**, 1135 (1969).
- [33] H. J. Jason Liu, G. A. Riley, C. L. Ordóñez-Romero, B. A. Kalinikos, and K. S. Buchanan, Time-resolved study of nonlinear three-magnon processes in yttrium iron garnet films, *Phys. Rev. B* **99**, 024429 (2019).
- [34] B. Kalinikos and A.N. Slavin, Theory of dipole-exchange spin wave spectrum for ferromagnetic films with mixed exchange boundary conditions, *J. Phys. C* **19**, 7013 (1986).
- [35] M. Mansuripur and R. Giles, Demagnetizing field computation for dynamic simulation of the magnetization reversal process, *IEEE Trans. Magn.* **24**, 2326 (1988).
- [36] I.S. Maksymov and M. Kostylev, Broadband stripline ferromagnetic resonance spectroscopy of ferromagnetic films, multilayers and nanostructures, *Physica E* **69**, 253 (2015).
- [37] See Supplemental Material at <http://link.aps.org/supplemental/10.1103/PhysRevB.107.L060401> for information on the methods and analyses employed, the derivation and linearization of our model, the calculation of the initial magnon amplitudes, and companion data at 2.5 GHz FMR frequency.
- [38] Matesy GMBH, <https://matesy.de/en/products/materials/yig-films>.
- [39] A. Y. Dobin and R. H. Victora, Intrinsic Nonlinear Ferromagnetic Relaxation in Thin Metallic Films, *Phys. Rev. Lett.* **90**, 167203 (2003).
- [40] V. Kambersky and C. E. Patton, Spin-wave relaxation and phenomenological damping in ferromagnetic resonance, *Phys. Rev. B* **11**, 2668 (1975).
- [41] Y.-H. Tang, N. Kioussis, A. Kalitsov, W. H. Butler, and R. Car, Influence of asymmetry on bias behavior of spin torque, *Phys. Rev. B* **81**, 054437 (2010).
- [42] N. A. Natekar, W.-H. Hsu, and R. H. Victora, Calculated dependence of FePt damping on external field magnitude and direction, *AIP Adv.* **7**, 056004 (2017).
- [43] W. F. Brown, Fluctuations of a single-domain particle, *Phys. Rev.* **130**, 1677 (1963).
- [44] Z. Liu, P.-W. Huang, G. Ju, and R. H. Victora, Thermal switching probability distribution of L10 FePt for heat assisted magnetic recording, *Appl. Phys. Lett.* **110**, 182405 (2017).
- [45] A. Venugopal, T. Qu, and R. H. Victora, Non-linear parallel pumped FMR: Three and Four magnon processes, *IEEE Trans. Microw. Theory Tech.* **68**, 602 (2020).
- [46] T. Qu, A. Venugopal, J. M. Etheridge, W. K. Peria, K. Srinivasan, B. J. Stadler, P. A. Crowell, and R. H. Victora, Non-linear magnon scattering mechanism for microwave pumping in magnetic films, *IEEE Access* **8**, 216960 (2020).